# Mechanical interaction among cells in hydrogel-based microfluidic assays

Lei Li<sup>1</sup>, Jiaqi Zhang<sup>2,3</sup>, Pengtao Yue<sup>4</sup>, and James J. Feng<sup>\*1,5</sup>

<sup>1</sup>Department of Chemical and Biological Engineering, University of British
Columbia, Vancouver, BC V6T 1Z3, Canada
 <sup>2</sup>Research Center for Mathematics, Advanced Institute of Natural Sciences,
Beijing Normal University, Zhuhai, 519087, China
 <sup>3</sup>Guangdong Provincial/Zhuhai Key Laboratory of IRADS, Beijing Normal-Hong
Kong Baptist University, Zhuhai 519087, China
 <sup>4</sup>Department of Mathematics, Virginia Tech, Blacksburg, VA 24061, USA
 <sup>5</sup>Department of Mathematics, University of British Columbia, Vancouver, BC
 V6T 1Z2, Canada

#### Abstract

Hydrogels are widely used in cell cultures and microfluidic organon-chip devices as a mimic for extracellular matrix. Soft and porous, they provide a gentle scaffold for the cell colonies to develop into properly structured tissues and organoids. A key factor in this process is the transmission of forces through the hydrogel, originating from the flowing perfusate and propagating toward and among the cells. Such forces serve as mechanical cues in the proliferation and differentiation of cells, and in their aggregation into functional organoids. In this work, we use a poroelastic model to study the mechanical interaction among cells that is mediated by the hydrogel. The model predicts that closely spaced cells induce the formation of prominent "tension ribbons" within the hydrogel, actively pulling neighboring cells together and prompting the development of mutual protrusions. In larger cellular arrays, the deformation patterns become highly heterogeneous, strongly dependent on the relative positions of individual cells. These insights provide valuable guidance for optimizing the design and operational parameters of organ-on-chip devices.

<sup>\*</sup>Corresponding author, james.feng@ubc.ca

# 1 Introduction

Hydrogels are ubiquitous in microfluidic-based cell cultures, organ-on-chip devices, and human disease models, where they perform several important functions as an *in vitro* replica for the extracellular matrix (ECM) [1–5]. Such synthetic gels typically have a low-density crosslinked polymer network that absorbs a large quantity of water. Being porous, hydrogels serve as a medium to deliver oxygen, nutrients and various growth factors from the perfusing stream to the cells. Equally importantly, they transmit mechanical stresses inside the hydrogel, from the flowing perfusate to the cells, and from one cell to another. Being soft, with a Young's modulus from tens of kPa down to hundreds of Pa [6], the gels typically carry a low stress level. Nevertheless, experiments have demonstrated significant consequences of even mild mechanical stimulations. For instance, mPa-level stresses can promote proliferation of endothelial cells [7] and differentiation of stem cells [8]. In liver-on-chip devices, shear stress on the mPa scale promotes albumin and growth factor production by hepatocytes [9], and stimulates their proliferation [10]. To elucidate the mechanotransduction in such microenvironments, we need to understand the fluid and solid mechanics in hydrogel-based cell cultures.

The gel-cell mixtures are typically highly heterogeneous in space, with widely divergent length scales. The gel itself is a mixture of a liquid solvent and a deformable solid network. The interstitial flow occurs on the pore scale, which typically ranges from a hundred nanometers to micrometers for synthetic hydrogels [11–13]. Embedded within this structure, the biological cells act as deformable inclusions. Upon inception of perfusion, the entire gel-cell mixture is subject to pressure and stresses emanating from the flow. The solvent, polymer network, and embedded cells each deform according to their individual mechanical properties, with close coupling among them. Even if we neglect the transmembrane exchange and various biochemical processes, the mere mechanics of the system presents a formidable challenge to mathematical modeling and computation.

Consequently, there have been relatively few studies of the mechanical factors governing the flow and deformation of a gel-cell system. In a tumor migration assay, Polacheck et al. [14] computed the Brinkman flow across a porous layer driven by a pressure drop, with a solid inclusion representing a cell. In a gel-filled chamber sheared by the perfusion flow, Bachmann et al. [15] computed the velocity field of a Newtonian fluid and the diffusion of a passive scalar, without embedded cells. Finally, Novak et al. [16] studied a shear-dominated flow in a three-dimensional bioreactor, with a spherical

inclusion representing a breast cancer cell. These efforts have offered insights into the flow and stress fields surrounding cells in a hydrogel. But the theoretical models have neglected key factors of the process, e.g., the fluid-to-gel interfacial transport and the deformability of the gel and the cells.

Recently, Li et al. [17, 18] sought a more faithful representation of the fluid and solid mechanics in a gel-cell mixture inside a microfluidic device, and developed numerical tools for simulating such systems under realistic flow conditions. In brief, the pore-scale process is coarse-grained into a poroelastic model, where the solvent and polymer skeleton are represented by their respective volume fraction, velocity and stress tensor. Each phase obeys its own continuity and momentum equations, with momentum exchange between the phases modeled by a linear Darcy drag law. The biological cell is treated as a hyperelastic object embedded inside the gel, subject to forces from the fluid and the skeletal phases. The interfacial exchange between the perfusing stream, which is a single-phase fluid, and the hydrogel is modeled by a set of boundary conditions (BCs) based on irreversible thermodynamics [19]. Specifically, these BCs consist in positing linear relations between interfacial jumps of shear and normal stresses on the one hand, and slip and permeation velocities on the other [20,21]. The dynamic changes of the computational domain, due to deformation and movement of the fluid-gel interface and the embedded cell, are handled by an arbitrary Lagrangian-Eulerian (ALE) scheme, which maps the deformed domain back to a reference frame via coordinate transformation [17].

Using the mathematical model and computational toolkit, Li et al. [18] studied the mechanics of a single cell embedded in a hydrogel, in a normal flow geometry mimicking the experiment of Polacheck et al. [14], as well as a shear flow geometry mimicking that of Novak et al. [16] and Bachmann et al. [15]. They found that the solvent flow deforms the hydrogel surface and injects the solvent into the gel, and that the interstitial flow deforms the polymer skeleton as well as the embedded cell. Among the three stress components, the pressure is the most potent in moving and deforming the cell, the elastic stress in the solid skeleton also plays a significant role, while the Brinkman stress due to the interstitial flow is the least important. The model also predicts mPa-level stresses transmitted to the cell, comparable to in vitro and in vivo data.

Although Li et al. [18] have gone beyond previous work in capturing the interstitial flow in the porous medium and the stress and strain sustained by the embedded cell, their model suffered from an obvious shortcoming: it only considered a single cell, and could not probe the mechanical crosstalk among the cells. That is the question that we set out to probe in this study.

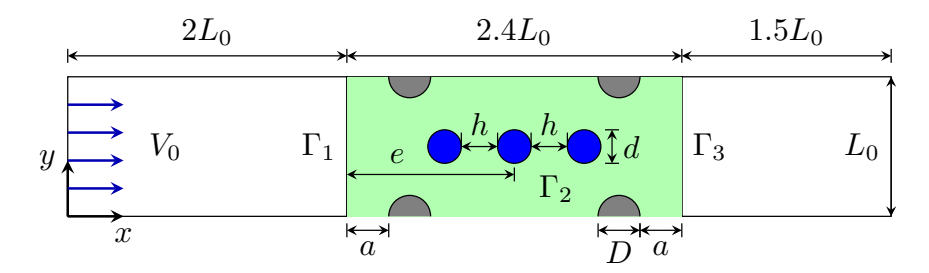


Figure 1: Geometric setup for our numerical simulations mimicking the microfluidic device of [14], with a gel layer (light green) held in place by solid posts (grey hemicircles). The embedded cells are shown as blue circles. The perfusion of the solvent is represented by a uniform flow coming from the left and passing normally through the gel-cell layer.

We extend their poroelasticity model by allowing multiple embedded hyperelastic cells in the gel matrix. Then we use finite elements to compute the dynamics of the coupled fluid-hydrogel-cell system in a normal-flow geometry motivated by the experiment of Polacheck et al. [14]. In analyzing the numerical simulations, we focus on how cells interact among themselves in simple regular arrays, e.g., doublets and triplets aligned with the flow direction or orthogonal to it, and in two-dimensional (2D) arrays of seven cells. The key finding is a "tension ribbon mechanism" between nearby cells, which tends to coordinate the cell movement and deformation by pulling them closer together.

# 2 Problem setup and methodology

## 2.1 Geometry

We base the 2D geometric setup of our simulations, shown in Fig. 1, on a microfluidic device of Polacheck et al. [14]. In essence, it consists in a gel layer separating two fluid channels at different pressures. The pressure drop drives a flow through the gel layer, normal to the gel surfaces. Though relatively simple, Fig. 1 captures the distinct features of interstitial flow in the original microfluidic device. In addition, we have simulated a shear-dominated geometry based on the device of Bachmann et al. [15]. In terms of cell-cell interaction, however, the shear-flow setup does not present fundamentally different mechanisms beyond those in the normal flow. Thus, we will only present results in the normal-flow geometry.

In the geometry of Fig. 1, the gel layer extends up and down in the y-

direction, and is held in place by the solid circular posts. The computational domain shown here is one repeating unit of the gel layer, with symmetry boundary conditions at the top  $(y = L_0)$  and bottom (y = 0). The perfusate flows with uniform velocity  $V_0$  normal to the gel layer, penetrates the upstream interface  $\Gamma_1$ , flows through the gel and exits the downstream interface  $\Gamma_3$ . The overall geometry is fixed with the post diameter  $D = 0.4L_0$ , and clearance  $a = 0.2L_0$ . One or several biological cell are embedded in the middle of the gel layer, with the gel-cell interface denoted by  $\Gamma_2$ . The initially undeformed cells have diameter  $d = 0.06L_0$  and radius  $r = 0.03L_0$ . The distance between the edges of adjacent cells is represented by h. Since r and h are relatively small compared to the characteristic length  $L_0$ , we adopt the cell radius r as the reference unit for quantifying h in subsequent discussions. We will vary h to study how cell-cell interaction affects their movement and deformation.

## 2.2 Problem formulation and numerics

The theoretical framework of this study largely follows that presented in our previous work [18] on single-cell mechanics. The only important difference here is the introduction of the additional geometric parameter h, the initial edge-to-edge spacing between neighboring cells. We model the hydrogel as a poroelastic continuum interacting with a viscous solvent, governed by continuity and momentum equations for each phase, complemented by appropriate interfacial boundary conditions derived from irreversible thermodynamics. For clarity and brevity, the full equations, boundary conditions, and scaling are detailed in Appendix A. The parameters of the problem are evaluated in Appendix B, with the baseline values summarized in Table 1. We will present results for these parameter values, with h being varied systematically.

The computations use the finite-element method of Li et al. [17] on the deal.II platform [22], with MPI-based parallelization [18]. A typical finite-element mesh is shown in Fig. 2, with Q2 quadrilateral elements, each edge being resolved by 3 nodes. The flow around the embedded cell and the elastic deformation inside the cell require refinement in and around it, and the fine mesh is illustrated in the blowup view. Because of symmetry, we only compute the upper half of the domain, with 5032 elements, 109921 degrees of freedom and the smallest mesh size  $h_{min} = 2.86 \times 10^{-3}$  (Fig. 2a). We have confirmed adequate temporal and spatial resolution by refining the mesh size and time step, with the minimum mesh size varying from  $3.65 \times 10^{-3}$  down to  $1.51 \times 10^{-3}$ , and the time step  $\Delta t$  from  $10^{-6}$  down to  $10^{-8}$ . All

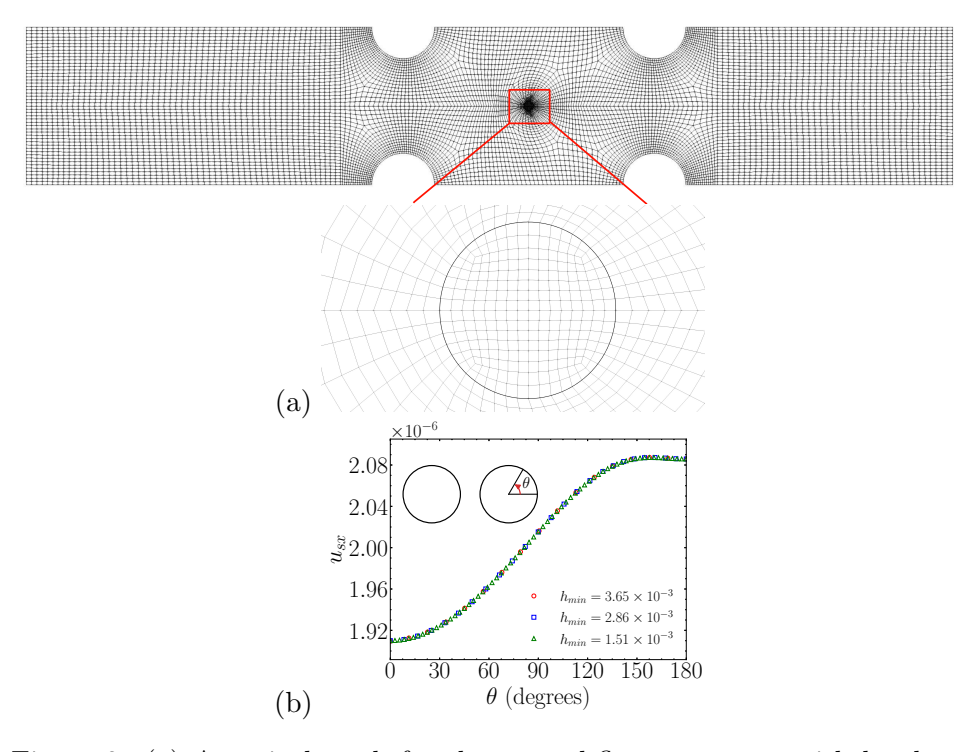


Figure 2: (a) A typical mesh for the normal-flow geometry, with local refinement around the cell embedded in the gel. The blowup shows details of the mesh inside and around the elastic cell. (b) Mesh convergence test using the streamwise displacement profile  $u_{sx}(\theta)$  around the downstream cell in a streamwise doublet at an edge-edge separation of r/3.

the variables of interest vary within 0.2%, with the maximum interstitial velocity  $v_{fx}$  varying by 0.119%, and the maximum interfacial displacement  $u_{sx}$  by 0.0175%. Figure 2(b) shows an example of such mesh-refinement tests for the streamwise doublet to be discussed in Sec. 3.1. The results reported below are based on the mesh of Fig. 2(a) with  $h_{min} = 2.86 \times 10^{-3}$  and time step  $\Delta t = 5 \times 10^{-8}$ . Because the cell areal change is small, approximating the cell area by inscribed polygons and taking the difference between pre- and post-deformation cell areas would both introduce large errors. Thus, special care has been taken in computing the cell shrinkage from the displacement of its boundary nodes. We use Newton iteration to solve the nonlinear system, with convergence defined as the  $L^2$  norm of the residual vector falling below a tolerance of  $10^{-10}$ . All simulations have been performed on a Linux workstation equipped with an Intel Core i9-13900 CPU. Most of the

simulation cases were completed within 6 hours.

# 3 Results and discussions

Even in the absence of any embedded cell, the gel deforms under the impingement of the solvent flow in the geometry of Fig. 1. With the realistic material and flow parameters used here (see Appendix B for parameter values), such deformation amounts to a strain on the order of  $10^{-6}$ . As intuitively expected, the gel displacement is predominantly streamwise, in the x-direction; it is larger in the center of the gel layer  $(y \sim 0.5)$  than toward the top (y=1) and bottom (y=0), where the solid stationary posts hamper gel displacement and deformation. In what follows, we first study two cells oriented along and normal to the flow direction, and then examine arrays of three and seven cells.

#### 3.1 Streamwise doublets

To form the streamwise doublet, we place a "test cell" at the center of the computational domain (at position e=1.2 in Fig. 1), and a "neighbor cell" either upstream or downstream with an initial edge-to-edge separation denoted as h. A positive h indicates that the neighbor cell is positioned downstream of the test cell, whereas a negative h implies the neighbor cell being upstream of the test cell. The interstitial flow around the doublet exhibits streamlines that resemble those for Stokes flow past two objects (Fig. 3a). Interestingly, between two closely apposed cells, as illustrated by Fig. 3(b) at h=-r/3, a pair of counterrotating vortices appear between them, similarly to Stokes flow past two nearby cylinders in tandem [23, 24]. The interstitial flow is essentially arrested in the region between the cells; the velocity magnitudes of Fig. 3(b) show that this is a "dead water zone" with negligible flow. In the following, we explore how the cell-cell interaction at different initial separations affects each cell's movement, deformation and the stresses inside and surrounding the cells.

#### 3.1.1 Cell displacement

Figure 4 plots the steady-state displacement of the centroid of the test cell as a function of the initial separation h. Although the positioning of the cells matters, their identity as test cell or neighbor does not. The test cell with an upstream neighbor behaves essentially identically to a downstream neighbor cell at the same separation |h|. The most obvious trend is that the

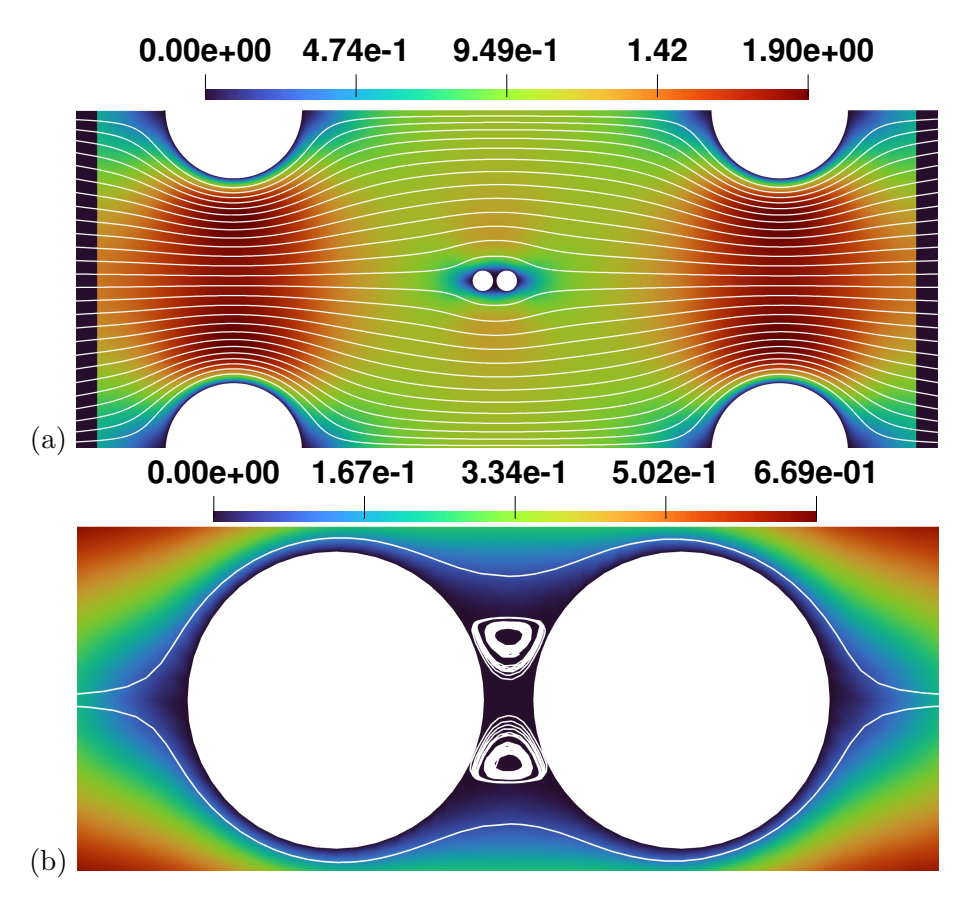


Figure 3: (a) Streamlines past a streamwise doublet placed on the centerline of the gel domain at initial separation h = -r/3, with color contours indicating the magnitude of the velocity. The test cell is at the center of the domain (e = 1.2), and the neighbor is upstream in this case. (b) Close-up of the recirculation between the two cells.

two cells appear to attract each other, such that an upstream neighbor tends to reduce  $u_x$  of the test cell, and a downstream neighbor tends to enhance it. This effect is intensified as the separation |h| shrinks. This apparent attraction between cells close to each other will be explained in terms of the "tension ribbon" in Sec. 3.1.2.

It is worth mentioning another intriguing feature of Fig. 4. The red dot marks the displacement of a single test cell, in the absence of a neighbor. Curiously, the single-cell displacement is not recovered as the neighboring cell is moved very far from the test cell. Instead, the red dot is below

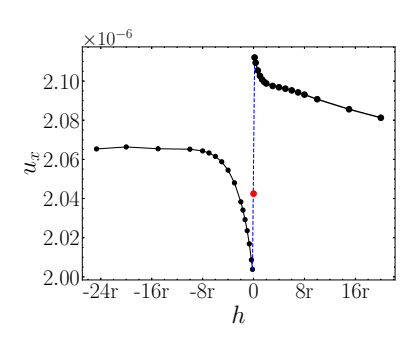


Figure 4: Streamwise displacement  $u_x$  of the centroid of the test cell, affected by the neighbor cell placed at different locations upstream (h < 0) and downstream (h > 0) of the test cell. The red dot marks the centroid displacement of the test cell if it were alone, without the neighbor.

the large-separation limit of a doublet. Numerical experiments show that other conditions being equal, placing a cell in the middle of the gel domain enhances the downstream displacement of the gel almost over the entire domain, in comparison with the all-gel domain. This can be understood from the fact that the cell is impermeable to the interstitial fluid. Thus, in comparison to the gel that would fill the same space, the cell receives a greater drag due to the pressure gradient as well as the fluid flow. As a result, the cell moves more downstream than the gel would, enhancing  $u_x$  overall. By the same token, having a second cell in the domain enhances the downstream movement  $u_x$  of the first cell, even if the two are far apart. When the neighbor is downstream (h > 0), an additional factor arises to boost  $u_x$  for the test cell: being upstream in the doublet configuration, the test cell receives greater pressure. This pushes the test cell even farther downstream than if the neighbor were absent.

#### 3.1.2 Tension ribbon

The apparent attraction between two cells in a streamwise doublet can be understood by examining the stresses acting on each cell. The total stress tensor in the hydrogel can be written as  $\sigma_t = -p\mathbf{I} + \phi_s \boldsymbol{\sigma}_s + \phi_f \boldsymbol{\sigma}_f$  (cf. Eqs. A.24 and A.25 in Appendix A), with contributions from the pressure, the solid stress and the fluid stress. Three observations that Li et al. [18] have made on single cells hold for the doublet as well. First, the pressure p and skeletal stress  $\phi_s \boldsymbol{\sigma}_s$  play major roles in moving and deforming the cell, whereas the Brinkman stress  $\phi_f \boldsymbol{\sigma}_f$  is at least one order of magnitude smaller, and can

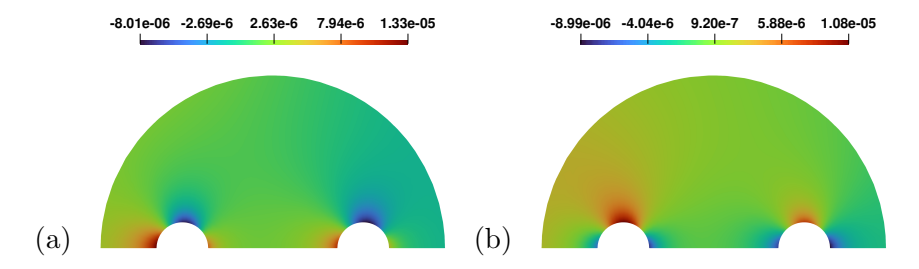


Figure 5: Contours of the normal stress components (a)  $\sigma_{sxx}$  and (b)  $\sigma_{syy}$  around the cells at h = -5r. For symmetry and clarity, only the upper half of the domain is plotted and only in a circular region around the two cells.

thus be ignored in a qualitative analysis. Of course, this does not mean that viscosity is unimportant. Its effect is mainly manifested by p via the Darcy drag. Second, upon onset of the flow, the immediate effect of p is to compress the cell so it contracts almost isotropically. Finally, the cell contraction pulls the surrounding gel radially inward, thus creating a tensile normal stress in  $\sigma_s$ .

These effects are apparent in Fig. 5 that plots the magnitude of the normal stress components around two cells relatively far apart (h = -5r). The contraction of each cell is reflected by the large tensile  $\sigma_{sxx}$  at its front and rear stagnation points, as well as the large tensile  $\sigma_{syy}$  on the apex of the cells. One may also note the compressive stresses  $\sigma_{sxx} < 0$  on the cell apexes, and  $\sigma_{syy} < 0$  at the stagnation points. These can be rationalized by the local gel strains. For example, at the top of the cells, the downstream movement of the cell squeezes the gel in the streamwise direction, producing a compressive strain  $\varepsilon_{sxx} < 0$ . At the front stagnation point, the cell movement requires gel displacement in the transverse direction toward the centerline, again producing a compressive  $\varepsilon_{syy} < 0$ .

As each cell contracts, they stretch the hydrogel in the gap between them. For smaller separations, this stretching intensifies as there is less gel material in the narrower gap. As a result, the local tensile strain increases, as does the tensile stress. This leads to the formation of a "tension ribbon" between the two cells, illustrated by Fig. 6 for a close separation of h = -r/6. The tensile stress explains the tendency, noted in Fig. 4, of the two cell centroids moving closer toward each other, even though their edge-to-edge distance gets larger due to cell shrinkage. As will be shown below, such tension ribbons are a prominent feature of cell-cell interactions in an array of cells embedded in a hydrogel. Incidentally, the tension ribbon coincides with the dead water zone between the cells in Fig. 3.

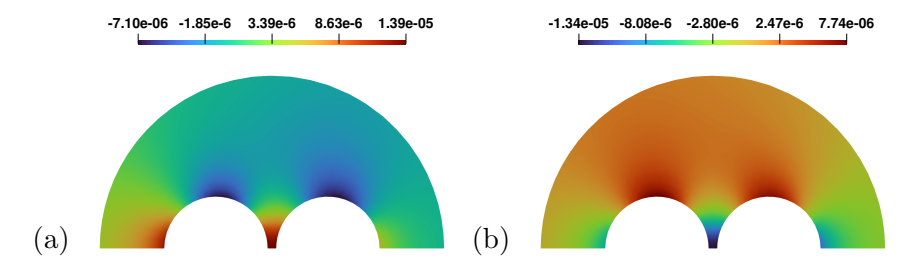


Figure 6: Contours of the normal stress components (a)  $\sigma_{sxx}$  and (b)  $\sigma_{syy}$  around the cells at h = -r/6. The "tension ribbon" forms between the two cells along the centerline, where the tensile stress  $\sigma_{sxx}$  attains a local maximum.

#### 3.1.3 Cell deformation and stress

As noted above, each cell individually would contract slightly in response to the hydrodynamic pressure in the gel that accompanies the interstitial flow. The contraction of the cell stretches the surrounding gel roughly radially inward, and such a radial tensile stress will resist the cell contraction [18]. Thus, the gel acts as a buffer layer to alleviate the action of the pressure. One may visualize this as the effect of elastic springs that tether the cell surface to the stationary posts that anchor the gel. This antagonism between the pressure and the gel stress turns out to be a general mechanism in the cellsin-gel system.

How does cell-cell interaction affect cell contraction? Figure 7 plots the steady-state area shrinkage of the neighbor cell and the test cell, with the neighbor being placed at different separations h upstream or downstream. Qualitatively, we can interpret the amount of cell shrinkage from the centerline pressure profile through the gel domain. The further upstream the neighbor cell, the higher pressure and hence greater shrinkage it experiences (Fig. 7a). But the steeper slope at greater |h| is due to a geometric anomaly, namely the proximity of the solid posts in Fig. 1. Approaching these posts, the neighbor cell experiences an expansion of the flow area and a pressure rise upstream and a contraction and a pressure drop downstream, which accentuate the changes in cell shrinkage.

The shrinkage of the test cell is somewhat subtler. There is strong asymmetry between positive and negative h values (Fig. 7b). As the neighbor is positioned further downstream, with h reaching 20r, it blocks the flow in the downstream contraction region, incurring a greater pressure drop. This raises the pressure upstream, and produces the sharp increase in the shrink-

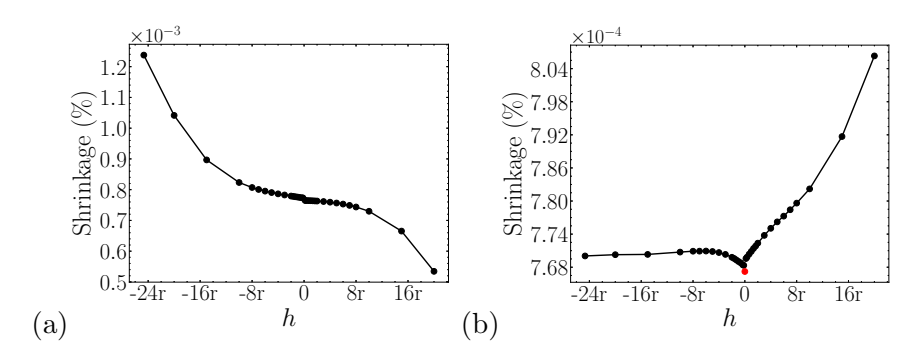


Figure 7: Shrinkage of (a) the neighbor cell, and (b) the test cell, as a percentage of the initial cell volume, as affected by the neighbor being placed upstream or downstream. The red dot marks the shrinkage of the test cell alone, in the absence of the neighbor.

age of the test cell. Conversely, when the neighbor is placed far upstream, it bears most of the increased pressure drop itself. The flow downstream past the test cell remains largely unaffected. Thus, the test cell shrinkage changes little for large negative h values. For small |h|, the tension ribbon pulls the two cells toward each other, and this reduces the shrinkage of both cells. Since two cells present greater resistance to the flow than a single cell, they entail a larger pressure drop. This explains why two cells shrink more than a single cell.

What role does the gel play in the above scenario? Figure 8 plots the pressure p, normal stress due to the solid skeleton  $\sigma_{snn} = \mathbf{n} \cdot (\phi_s \boldsymbol{\sigma}_s) \cdot \mathbf{n}$  and the total normal stress  $\sigma_{tnn} = \mathbf{n} \cdot \boldsymbol{\sigma}_t \cdot \mathbf{n}$  around the two cells. The Brinkman normal stress, due to  $\phi_f \sigma_f$ , is about three orders of magnitude smaller than p and the solid normal stress, and can thus be safely ignored. As expected, we see in Fig. 8(a) a consistently higher pressure on the upstream cell regardless of the separation h. But Fig. 8(b) shows that the surrounding gel provides such a reaction as to neutralize most of the pressure differential. As a result, the total normal stress is roughly symmetric for the two cells in Fig. 8(c). In fact, at the large separation h = -5r, the cancellation effect is also local in the sense that  $\sigma_{tnn}$  is largely uniform around the cell. Thus, the gel provides a buffer to shield the cells from the pressure. Where a high pressure compresses a cell, the surrounding gel gets stretched to offer additional resistance to the compression. Finally, at close proximity, Fig. 8(d) shows a mild protrusion of each cell toward the other, thanks to the tension ribbon between the two.

One can also roughly estimate the cell shrinkage from the bulk modulus

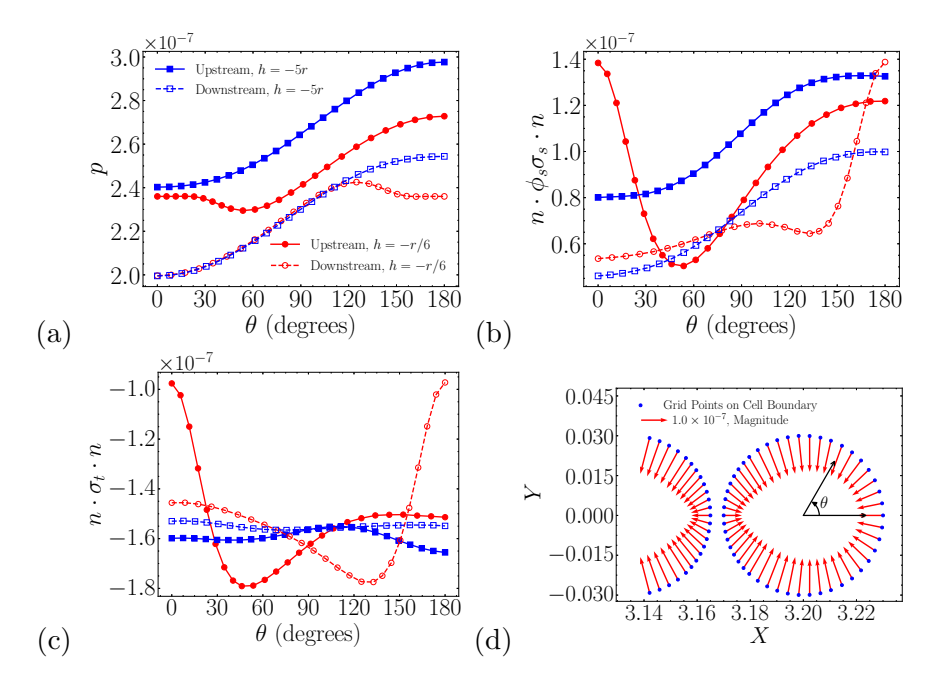


Figure 8: Normal stress profiles around the cells, with the polar angle  $\theta$  defined in panel (d). (a) Pressure p for the test cell downstream and the neighbor upstream, at h = -r/6 and -5r. (b) Similar comparison of the normal stress due to the solid stress tension  $\phi_s \sigma_s$ . (c) Similar comparison of the total normal stress  $\mathbf{n} \cdot \sigma_t \cdot \mathbf{n}$ . (d) Deformation of the test cell at h = -r/6, depicted by the displacement vectors of the cell boundary points toward the cell centroid. The length of these vectors have been exaggerated for a clearer view, and the red arrow in the legend provides a scale bar for their magnitude. The rear of the upstream neighbor is also shown to indicate the proximity between the two.

of the cell ( $K_c = \mu_c + \lambda_c = 0.02$  in dimensionless form) and the normal stresses on it. For example, at h = -5r, the average normal stress is about  $-1.6 \times 10^{-7}$  from Fig. 8c). The expected areal contraction is thus  $8 \times 10^{-6}$ , consistent with the numerical data of Fig. 7.

The interaction between the cells also affects the stress and strain inside the cells. Figure 9 compares the distribution of the von Mises stress (defined in Eq. A.12) inside both cells for two cell-cell separations. When the cells are far apart (h = -5r), the compressive strain and stress are largely uniform inside each cell, with a small advantage to the upstream face of the cell. This is similar to the case of a single cell [18]. As |h| decreases, the tension ribbon

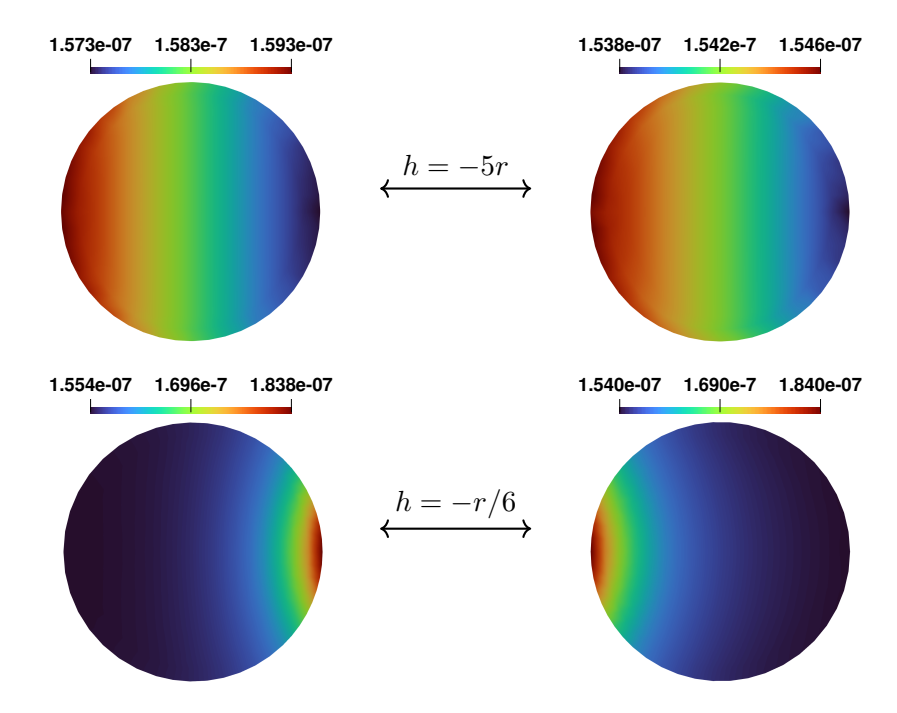


Figure 9: Distribution of von Mises stress inside both cells at h = -5r (top row) and h = -r/6 (bottom row). Note the shift in the maximum stress in the upstream cell as the two get closer, as well as the greater spatial variations in stress magnitude.

between the cells pulls on the rear face of the upstream cell, and shifts the maximum stress inside the cell from the upstream to the downstream face. Similarly, the tension ribbon strengthens and localizes the stress maximum in the downstream cell at its upstream stagnation point. Thus, in both cells, the von Mises stress peaks at their surface points facing the narrow gap. This localization of strain and stress also implies greater spatial inhomogeneity inside each cell, apparent from the widening range of von Mises stress with smaller |h|.

# 3.2 Streamwise triplets

In discussing the streamwise doublet, we have found it convenient to designate one cell as the "test cell", and the other as the upstream or downstream "neighbor", distinguished by the sign of the edge-to-edge separation h. In dealing with triplets and multiple cells, however, the relative positioning

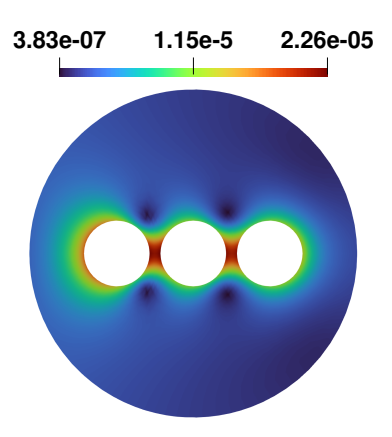


Figure 10: Tension ribbons in a streamwise triplet at h = r/3, shown by color contours of the von Mises stress computed from the gel elastic stress tensor  $\sigma_s$ . The central cell is initially placed at the center of the domain (e = 1.2).

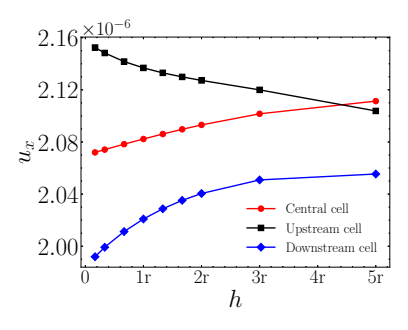


Figure 11: Displacement of three cells in a streamwise triplet: dependence on the initial edge-to-edge separation h.

is more complex and will be described more explicitly. As a result, we no longer rely on the sign of h to distinguish up- and downstream. Hereafter, we will use h only as a positive number that represents the initial edge-to-edge distance.

The streamwise triplet is similarly dominated by the tension ribbons when the cells are close to one another. Such ribbons are illustrated by the stress contours of Fig. 10. The streamwise displacement of the centroids of the 3 cells are shown in Fig. 11 as functions of h; their behavior can be understood from the tension ribbons. At any initial separation h, all three cells move downstream ( $u_x > 0$ ). With decreasing h, the upstream cell moves farther downstream while the other two show smaller displacements.

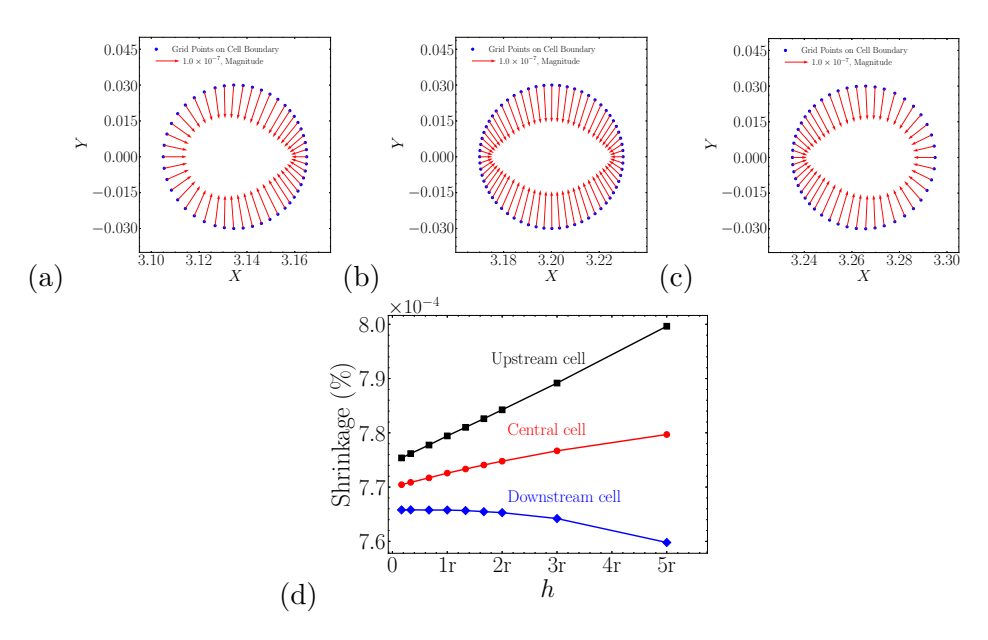


Figure 12: Shrinkage of three cells in a streamwise triplet. (a, b, c) Deformation of the upstream neighbor, central cell, and downstream neighbor depicted by the displacement vectors of the cell boundary points toward the cell centroid; initial edge-to-edge separation h = r/6 in all three panels. (d) Areal shrinkage of the three cells at different initial h values.

As the difference in  $u_x$  diverges between cells with decreasing h, the three cells are being pulled closer together by the tension ribbon, similarly to the doublet of Fig. 4. The magnitudes of the displacements and their variations with h are comparable with those of the doublet.

How do the tension ribbons affect cell deformation? As h decreases, the tension ribbons pull on the up- and downstream cells in a way similar to that in a streamwise doublet. Each shows a mild protrusion toward the central cell (Fig. 12a,c), reminiscent of the doublet deformation shown in Fig. 8(d). The central cell, being stretched on both ends, extends protrusions to both sides (Fig. 12b) and sustains more strain and stress than its neighbors. Its maximum von Mises strain and stress (not shown) are also somewhat higher than the cells in the doublet, and this difference increases with decreasing h. In terms of the cell area change, an upstream cell shrinks more than a downstream one (Fig. 12d), as expected. With decreasing h, the upstream and central cells see reduced shrinkage, mainly thanks to the tension ribbons. For the upstream cell, its position shifts downstream at

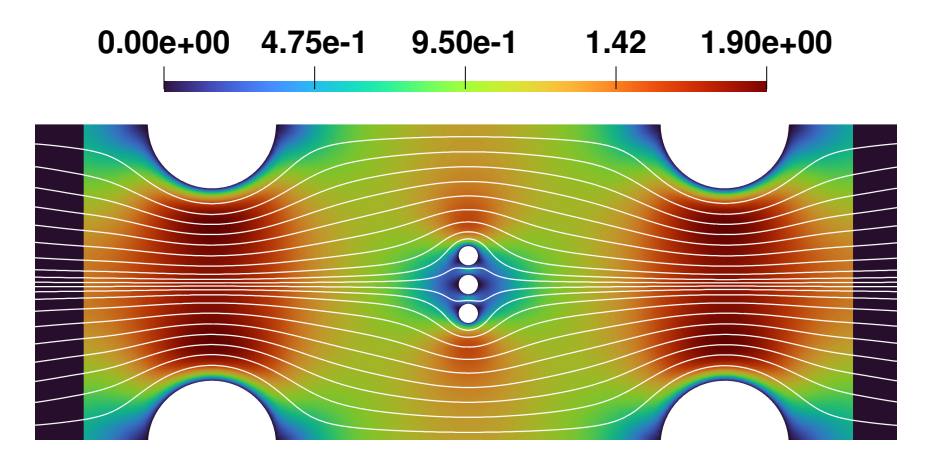


Figure 13: Streamlines past a triplet of cells aligned perpendicular to the flow direction, at a cell-cell separation h = r/3. The central cell is initially placed at the center of the domain (e = 1.2).

smaller h, and thus it experiences a lower pressure. This also contributes to its diminishing shrinkage. For the downstream cell, on the other hand, the advantage in positioning apparently compensates for the stress ribbon; its shrinkage increases somewhat with decreasing h.

#### 3.3 Transverse triplets

For a transverse triplet placed in the middle of the gel domain, the streamlines again resemble a Stokes flow around obstacles in pure fluid (Fig. 13). Much as in Stokes flow, the transverse triplet reduces the flow area of the cross section, and produces a "blockage effect". With the reduction of flow area comes an elevated pressure upstream of the cells. A consequence is that the transverse triplet moves downstream more than the streamwise triplet (Fig. 14a). As expected, the center cell receives a stronger push than the two edge cells, exhibiting a larger displacement  $u_x$ . With decreasing cell separation h,  $u_x$  initially increases, but then declines for the tighter triplets, suggesting an optimal separation for catching the most blockage effect. Conceivably, there is a tradeoff between the fluid going around the triplet as a whole and that going through the gaps between the cells.

Perhaps contrary to hydrodynamic expectations, the top and bottom cells do not move transversely away from the central one; they shift slightly inward instead (Fig. 14b). This is no real surprise, now that we know the prominent role of the tension ribbon among nearby cells. Figure 15 depicts

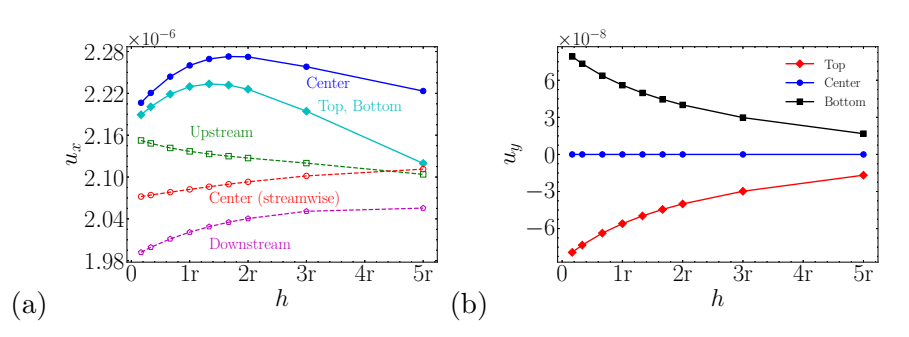


Figure 14: (a) Streamwise displacement  $u_x$  for the transverse triplet, in comparison with the streamwise triplet (dashed curves). (b) Transverse displacement  $u_y$ . The top and bottom cells move toward the center cell.

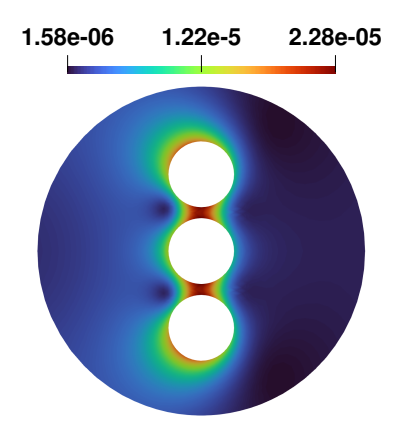


Figure 15: Tension ribbons in a transverse triplet at h = r/3, shown by color contours of the von Mises stress computed from the gel elastic stress tensor  $\sigma_s$ .

the tension ribbons in terms of the von Mises stress of the gel total stress tensor  $\phi_s \sigma_s$ . The origin of the tension ribbons is the same as in the streamwise arrays (Fig. 10). As the neighbors get close, their individual contraction engenders strong stretching in the gap between them. Generally, the tension ribbons tend to be slightly stronger in the transverse configuration than in the streamwise one. For example, the maximum von Mises stress among the transverse triplet reaches  $2.28 \times 10^{-5}$  at h = r/3, compared with  $2.26 \times 10^{-5}$  in the streamwise triplet at the same h.

Finally, we examine the effect of the gel stresses on the three cells in the transverse triplet (Fig. 16). The three cells shrink essentially the same amount, and it is generally greater than that of the streamwise triplet, man-

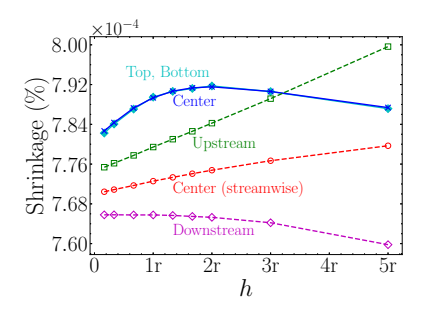


Figure 16: Shrinkage of the cells in the transverse triplet at different initial separation h. The shrinkage of the streamwise triplet is also shown in dashed curves for comparison.

ifesting the higher pressure sustained by the transverse triplet owing to the blockage effect. With increasing h, the shrinkage initially increases, probably due to the weakening tension ribbons. But past h = 2r, the trend is reversed. This behavior mirrors that of the displacement  $u_{sx}$  in Fig. 14(a), again suggesting an optimal blockage effect at an intermediate h.

# 3.4 Two-dimensional cell arrays

We have tested the behavior of a regular hexagonal array of 7 cells placed initially at the center of the gel domain (Fig. 17). At large separations, e.g. h=2r of Fig. 17(a), the cells interact little among themselves, and each cell's movement and deformation is similar to that of an isolated cell. The dominant feature is the individual contraction of each cell, which stretches the surrounding gel and produce a tension ring. The gap between each trio of cells, e.g., Cells 1, 2, 4, sustains relatively small stress, and thus present the hexagonal pattern of blue circles in the plot. If the cells are closer to each other, e.g., at h=r/3, tension ribbons appear between neighbors, producing the regular pattern of high stresses in Fig. 17(b). This is the most important phenomenon for cell arrays, and affects the movement and deformation of individual cells. Moreover, the fluid flow is severely suppressed in the gap between the cells. For h=r/3, for example, we observe dead water zones in the interior of the cell array (not shown), with recirculation similar to Fig. 3(b).

In a tightly spaced array, the tension ribbons tend to pull the array even closer together. This is clearly demonstrated by the centroid displacement for the seven cells in Fig. 18. Note first the non-monotonic variations of  $u_x$  with h (with the exception of the trailing Cell 3). With decreasing h,  $u_x$ 

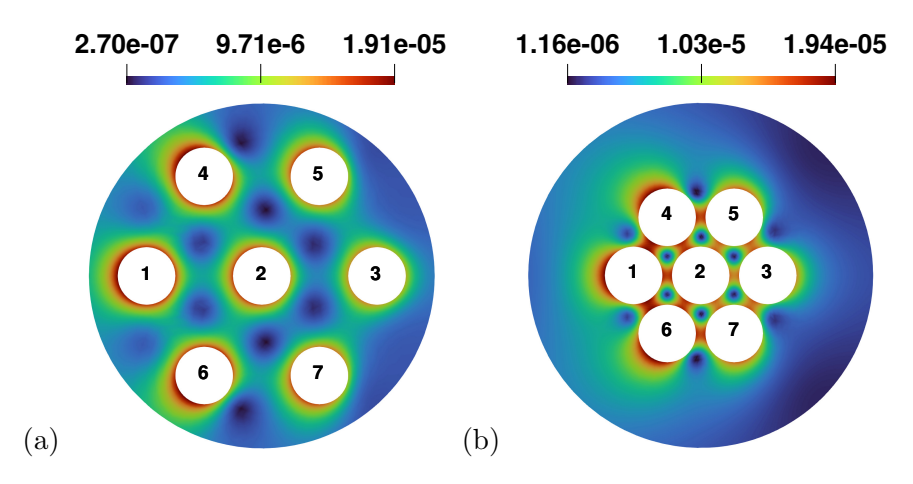


Figure 17: Distribution of von Mises stress for the gel elastic stress  $\sigma_s$  around the cell array with initial cell-cell separation (a) h = 2r, (b) h = r/3. The central cell is initially placed at the center of the domain (e = 1.2). Note the sharpening of the tension ribbons between the cells as they get closer to one another.

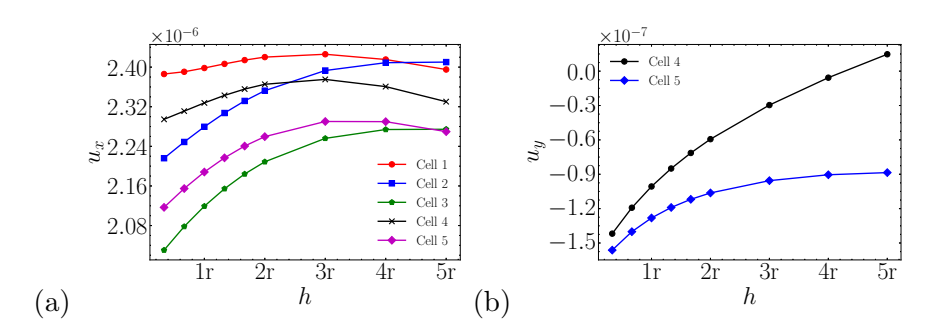


Figure 18: Steady-state displacement of the cells in the 2D array as function of the initial separation h. (a) Streamwise displacement  $u_x$ . For symmetry only the top Cells 4 and 5 are plotted together with the central Cells 1–3. (b) Transverse displacement  $u_y$  for the outer Cells 4, 5.

tends to increase first and then decrease for all cells. This trend is essentially the same as previously seen in the transverse triplet of Fig. 14(a), reflecting a subtlety in the blockage effect. Secondly, at the smaller h values,  $u_x$  is always greater for a cell that is more upstream, in the decreasing order of Cell 1, 4, 2, 5, and 3. This implies that the cells are moving inward along the flow direction. Similar inward movement can be seen in the transverse direction in Fig. 18(b). Thus, the tension ribbons pull an initially close array

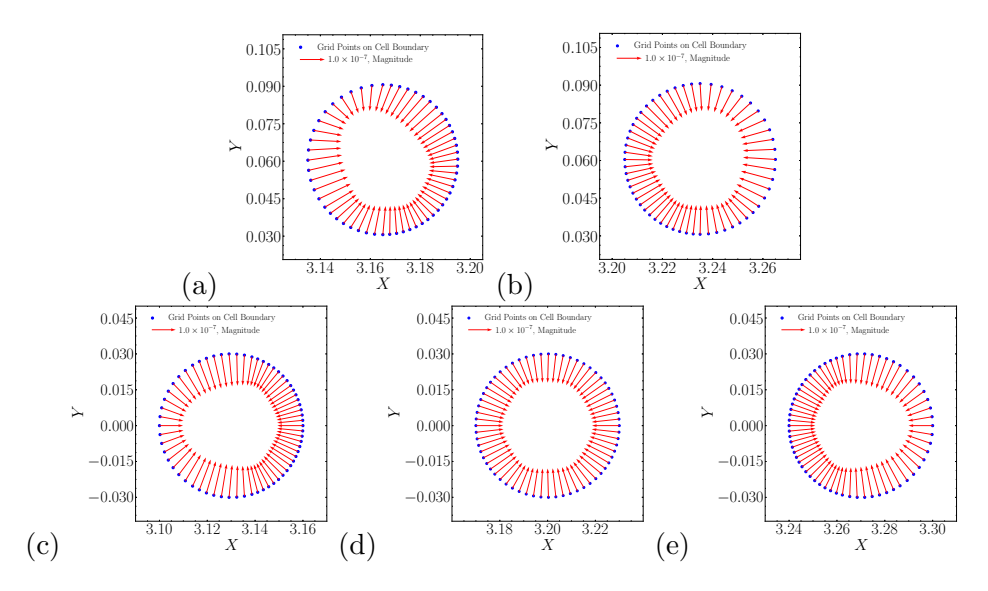


Figure 19: Cell deformation indicated by displacement of boundary nodes relative to the centroid at h=r/3. Panels (a)–(e) are arranged spatially in the same pattern as the Cells 1–5 labeled in Fig. 17(a); e.g., panels (c)–(e) correspond to Cells 1–3.

further inward. It is also interesting to compare  $u_x$  of the 2D array with that for the streamwise triplet. The 2D array moves farther downstream than the triplet, by some 10%. This is another manifestation of the blockage effect, noted in Fig. 14(a) already.

The cell deformation also bears clear signature of the tension ribbons. Part of the cell boundary closest to a nearby neighbor shrinks less inward because of the stretching toward that neighbor. Thus, the boundary displacement vectors for Cell 1 exhibit three such protrusions toward its three neighbors, Cell 2, 4 and 6 (Fig. 19a). Similar protrusions toward neighbors can be seen for all other cells in Fig. 19. In particular, the central Cell 2 is being pulled by six neighbors.

The shrinkage is greater for cells positioned more upstream (Fig. 20), following the decreasing order of Cell 1, 4, 2, 5, 3, much as the cell displacement of Fig. 18. In the range of h tested, the cell shrinkage in the 2D array largely resembles that of the streamwise triplet (Fig. 12). The shrinkage increases with h thanks to the diminishing tension ribbon, with the farthest downstream Cell 3 exhibiting a decreasing trend at larger h similar to the downstream cell of the streamwise triplet. In comparison with the transverse triplet (Fig. 16), one wonders if the blockage effect also maximizes at a

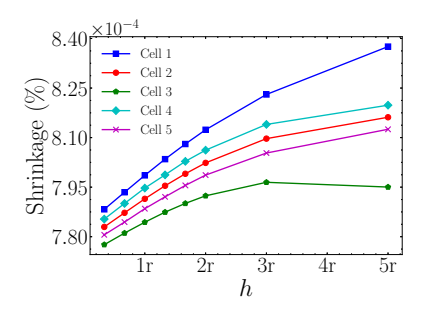


Figure 20: Shrinkage of the cells in the 2D array as function of the initial cell-cell separation h.

certain intermediate h. The curves of Fig. 20 suggests that such a maximum may exist at a greater separation than 5r.

To summarize our findings for all the cell arrays, we point to the tension ribbon as the most important mechanism of cell-cell interactions. Their principal effect is to pull the cells inward more tightly. They also deform the cells, pulling out protrusions toward one another. This typically counters cell shrinkage. The transverse and 2D cell arrays also exhibit a blockage effect, which produces higher pressure on the cells because of the reduction in cross-sectional flow area. There seems to be a maximum blockage effect at a moderate cell-cell separation, where the cell array is best able to catch the impact of the interstitial flow.

Is the mechanical interaction among cells strong enough to induce biochemical responses from the cells? Granted, for ease of analysis we have only studied small arrays of a few cells. Extrapolating our findings to larger cell colonies, we expect strong tensile stresses and suppressed fluid flow in the interior of the cell ensembles. Both may have implications for the viability and behavior of the interior cells. Larger stress may induce proliferation or differentiation of the cells [10, 16, 25], and may even cause apoptosis [26,27]. To give a quantitative idea, the tension ribbons in the 2D array at h = r/3 feature a von Mises stress ranging up to 12.7 mPa. This level of mechanical stimulation is more than adequate to induce biochemical changes inside cells, and affect the evolution and fate of a cell colony. For example, Long et al. [9, 10] have examined how hepatocytes react to shear stress due to perfusion, and found that an intermediate level of stress around 5 mPa produces optimal hepatocyte proliferation. Lack of fluid perfusion may also imply privation of oxygen, nutrients, as well as necessary growth factors [4,9,15,28,29]. These remain to be studied in a more realistic setup

for larger cell ensembles.

# 4 Conclusion

Microfluidic organ-on-chip devices typically feature cell colonies developing in a hydrogel-based matrix, a process that is as sensitive to mechanical cues in the hydrogel environment as to biochemical ones. This work studies the mechanical interaction among the perfusing fluid, the elastic skeleton of the hydrogel and the embedded cells, with an emphasis on the cell-cell interactions.

The most important observation is that when cells are initially closely packed in a gel, they form tension ribbons among them, which tend to pull the array even more closely together. This may have important implications to the performance of the organ-on-chip device, and even the survival of cell culture. On the one hand, the mechanical stress can stimulate cell proliferation and tissue regeneration [9,10]. On the other, it could further reduce the penetration of nutrients and growth factors into the center of the cell colony, potentially suppressing cell growth and even inducing necrosis.

Our work is based on a continuum-level poroelasticity model, and necessarily involves various simplifications to facilitate the analysis. It is important to recognize these simplifications as one seeks to apply such modeling to individual devices. First, we have considered a relatively simple 2D geometry representing a biomicrofluidic device. Three dimensionality and other geometric features may introduce new mechanisms for cell-cell interactions that are not accounted for here. Second, we have included only a small number of cells in our simulations, and the effects remain to be explored and confirmed in more realistic larger cell colonies. Third, we have modeled the cells as compressible neo-Hookean solids. In reality, a cell is a highly heterogeneous and complex object, with transport of water, ions and various proteins across the membrane. Under compressive normal stresses, the water is squeezed out of the cell and thus the cell volume shrinks [30]. In particular, it has been observed that the cell membranes may be temporarily compromised to allow cytosol leakage under rapid forcing [31,32]. Our model represents this shrinkage effect indirectly by the effective elastic moduli of the model cell. But it is unclear if the time scale of cell shrinkage [32] is well represented by that of the elastic shrinkage. Therefore, our treatment must be viewed as a first approximation, whose accuracy should be verified and improved upon by more sophisticated models. Finally and perhaps most significantly, we have ignored the potential for cells to remodel themselves

under mechanical stimulation and to restructure the surrounding polymer matrix. For example, the stiffness of the surrounding gels can affect the differentiation and fate of stem cells, with softer gels favoring production of adipocytes and harder ones osteoblasts [33], through a pathway that links cytoskeletal force sensing to gene expression [34]. Not only do cells remodel and proliferate, thereby changing their own properties, but they also actively remodel the surrounding matrix, e.g., by degrading matrix proteins using metalloproteinases [35]. This two-way coupling between the extracellular matrix and the cells will certainly affect the mechanical interactions between the two.

In view of the above, the model should be validated against experimental data. Currently there is a dearth of comparable data, probably owing to technical challenges in measuring the forces within cell colonies inside a gel matrix. Progress can be made by conducting experiments in simplified geometries and flow conditions, where cell deformation can be recorded and used to back out the stresses on the cells. Such data can serve as benchmarks to validate the predictions of the current model.

Despite its limitations, this work provides a theoretical basis and computational tools for analyzing cell-cell and cell-gel mechanical interaction in microfluidic systems. Such mechanical cues play important biochemical roles, e.g., in the development of organoids and artificial tissues in vitro [9, 10], and in embryogenesis in vivo [36,37]. Therefore, our work represents a step toward understanding such processes, especially in hydrogel-based cell cultures in microfluidics and organ-on-chip devices. With certain modifications and refinements, the model and computational tools developed here may also apply to in vivo scenarios of cells in gel-like extracellular matrices.

# 5 Acknowledgements

We acknowledge financial support by the Natural Sciences and Engineering Research Council of Canada (Discovery Grant No. 2019-04162, 2024-03982, Alliance International Grant No. 586462-23) for J.J.F., by the National Science Foundation (Grant DMS2309732) for P.Y., and by the Natural Science Foundation of China (Grant No. 12401511), the Guangdong Basic and Applied Basic Research Foundation (Grant No. 2023A1515110861), and Guangdong Provincial Key Laboratory of IRADS (2022B1212010006) for J.Z. We thank Yu Du, Mian Long, Amir Reza Mohebi and Zelai Xu for helpful discussions.

# Appendix A Theoretical formulation

# A.1 Governing equations

In our formalism, the hydrogel is an effective continuum made of the solvent phase of volume fraction  $\phi_f$  and the solid network phase of volume fraction  $\phi_s = 1 - \phi_f$ . Each phase obeys its own volume-conservation and momentum equations:

$$\frac{\partial \phi_s}{\partial t} + \nabla \cdot (\phi_s \mathbf{v}_s) = 0, \tag{A.1}$$

$$\nabla \cdot (\phi_s \mathbf{v}_s + \phi_f \mathbf{v}_f) = 0, \tag{A.2}$$

$$\nabla \cdot (\phi_f \sigma_f) - \phi_f \nabla p + \xi \phi_f \phi_s (\mathbf{v}_s - \mathbf{v}_f) = 0, \tag{A.3}$$

$$\nabla \cdot (\phi_s \sigma_s) - \phi_s \nabla p + \xi \phi_f \phi_s (\mathbf{v}_f - \mathbf{v}_s) = 0, \tag{A.4}$$

$$\frac{d\mathbf{u_s}}{dt} - \mathbf{v_s} = 0,\tag{A.5}$$

where  $\mathbf{v}_f$  and  $\mathbf{v}_s$  are the phase-averaged velocities of the fluid and solid phases,  $\sigma_f$  and  $\sigma_s$  are their Cauchy stress tensors, p is the shared pressure, and  $\mathbf{u}_s$  is the displacement of the solid phase in the hydrogel. The momentum exchange between the phases is via the Darcy drag terms, with a constant drag coefficient  $\xi$ . Note that Eq. (A.1) is the continuity of the solid phase. A similar one can be written for the fluid phase, but in its place, we have used the sum of the two in Eq. (A.2).

The solvent is a viscous fluid of viscosity  $\mu$ , with a Brinkman stress tensor  $\sigma_f = \mu[\nabla \mathbf{v}_f + (\nabla \mathbf{v}_f)^T]$ . The solid network obeys the neo-Hookean model:

$$\sigma_s = \mu_s J^{-1}(\mathbf{F} \cdot \mathbf{F}^T - \mathbf{I}) + \lambda_s (J - 1)\mathbf{I}, \tag{A.6}$$

where **F** is the deformation gradient,  $J = \det(\mathbf{F})$  is its determinant, **I** is the unit tensor, and  $\lambda_s$  and  $\mu_s$  are the Lamé parameters related to Young's modulus E and Poisson's ratio  $\nu$  as follows:

$$\lambda_s = \frac{E\nu}{(1+\nu)(1-2\nu)}, \quad \mu_s = \frac{E}{2(1+\nu)}.$$
(A.7)

From **F** we compute the Green-Lagrangian strain tensor  $\mathbf{E} = (\mathbf{F} \cdot \mathbf{F}^T - \mathbf{I})/2$ , and use its components to analyze the hydrogel and the cell deformation in the main text.

For the flow of the viscous solvent outside the gel, we neglect inertia and pose the Stokes equation for the exterior velocity V and the pressure P:

$$\nabla \cdot \mathbf{V} = 0, \tag{A.8}$$

$$\nabla \cdot \mathbf{\Sigma} - \nabla P = 0, \tag{A.9}$$

where  $\Sigma = \mu[\nabla \mathbf{V} + (\nabla \mathbf{V})^T]$  is the viscous stress tensor,  $\mu$  being the solvent viscosity.

The embedded cells are also modeled as hyperelastic neo-Hookean solids, with Lamé constants  $\lambda_c$  and  $\mu_c$  and a Cauchy stress tensor  $\sigma_c$ . We describe the cell deformation and movement using the displacement field  $\mathbf{u}_c$  and velocity field  $\mathbf{v}_c$  inside the cell, which evolve according to

$$\nabla \cdot \boldsymbol{\sigma}_c = 0, \tag{A.10}$$

$$\frac{d\mathbf{u}_c}{dt} - \mathbf{v}_c = 0. (A.11)$$

As a representation of the intensity of the stress in the gel or inside the cell, we define a scalar von Mises stress from the components of the stress tensor in 2D planar geometry. Take the cell stress  $\sigma_c$  for example:

$$\sigma_{cv} = \sqrt{\sigma_{cxx}^2 + \sigma_{cyy}^2 - \sigma_{cxx}\sigma_{cyy} + 3\sigma_{cxy}^2}.$$
 (A.12)

A von Mises strain can be similarly defined as a scalar representation of the intensity of deformation in the gel or inside the cell.

## A.2 Boundary conditions

Because of symmetry, only the upper half of the domain of Fig. 1 will be computed. On the bottom (y = 0) and the midline  $(y = 0.5L_0)$  of the domain, symmetric conditions are used, with  $\partial/\partial y = 0$ . On the surface of the solid posts, the interstitial flow and the solid displacement both vanish:  $\mathbf{v}_f = \mathbf{0}$ ,  $\mathbf{u}_s = \mathbf{0}$ . On the entry on the left, we impose a uniform velocity  $V_0$ . On the exit on the right, we employ the zero-stress natural boundary condition.

On the fluid-gel interfaces  $\Gamma_1$  and  $\Gamma_3$ , we impose the boundary conditions BC2 in the following form [19]:

$$\mathbf{V} - \mathbf{v}_s = \phi_f(\mathbf{v}_f - \mathbf{v}_s) \cdot \mathbf{n},\tag{A.13}$$

$$(-p\mathbf{I} + \phi_f \boldsymbol{\sigma}_f + \phi_s \boldsymbol{\sigma}_s) \cdot \mathbf{n} = (-P\mathbf{I} + \boldsymbol{\Sigma}) \cdot \mathbf{n}, \tag{A.14}$$

$$(\mathbf{V} - \mathbf{v}_f) \cdot \mathbf{n} = \eta \mathbf{n} \cdot [(\mathbf{\Sigma} - P\mathbf{I}) - (\boldsymbol{\sigma}_s - p\mathbf{I})] \cdot \mathbf{n}, \tag{A.15}$$

$$(\mathbf{V} - \mathbf{v}_f) \cdot \mathbf{t} = \beta(\mathbf{\Sigma} \cdot \mathbf{n}) \cdot \mathbf{t}, \tag{A.16}$$

$$\phi_s(\mathbf{v}_s - \mathbf{v}_f) \cdot \mathbf{t} = -\beta(\boldsymbol{\sigma}_s \cdot \mathbf{n}) \cdot \mathbf{t}, \tag{A.17}$$

where **n** is the normal vector pointing outward from the gel toward the fluid,  $\eta$  is an interfacial permeability, and  $\beta$  is an interfacial slip coefficient. On

interfaces  $\Gamma_2$  separating the hydrogel and the cells, we impose continuity of displacement, velocity and normal traction:

$$\mathbf{v}_s = \mathbf{v}_f = \mathbf{v}_c, \tag{A.18}$$

$$\mathbf{u}_s = \mathbf{u}_c,\tag{A.19}$$

$$\boldsymbol{\sigma}_c \cdot \mathbf{n} = (\phi_s \boldsymbol{\sigma}_s + \phi_f \boldsymbol{\sigma}_f - p\mathbf{I}) \cdot \mathbf{n}. \tag{A.20}$$

where **n** represents the normal vector to  $\Gamma_2$ .

### A.3 Scaling and dimensionless parameters

Referring to Fig. 1, we take  $L_0$  to be the characteristic length  $L_0$  and  $L_0/V_0$  to be the characteristic time. Furthermore, we adopt  $\mu_s$  for the hydrogel solid network as the characteristic stress. With these three characteristic quantities, all variables and parameters of the problem, as well as the governing equations and boundary conditions, can be made dimensionless. Out of the geometric and physical parameters, we can extract the following 10 dimensionless groups, each denoted by an overbar,

$$\bar{e} = e/L_0, \bar{h} = h/L_0, \bar{\lambda}_s = \lambda_s/\mu_s, \bar{\lambda}_c = \lambda_c/\mu_s, \bar{\mu}_c = \mu_c/\mu_s,$$

$$\bar{\xi} = \xi L_0^2/\mu, \bar{\eta} = \eta \mu/L_0, \bar{\beta} = \beta \mu/L_0, Ca = V_0 \mu/(L_0 \mu_s), \phi_{s0},$$
(A.21)

where  $\phi_{s0}$  is the initial solid fraction in the undeformed hydrogel. Ca indicates the ratio between the external viscous stress and the elastic stress of the solid skeleton, and can be viewed as an effective capillary number. Besides, certain length ratios are fixed for the rest of the paper, including  $\bar{a} = 0.2$ ,  $\bar{D} = 0.4$ ,  $\bar{d} = 0.06$  and other ratios indicated in Fig. 1.

Since the main text uses mostly dimensionless variables, we will drop the

overbar for simplicity. The dimensionless governing equations are as follows:

$$\frac{\partial \phi_s}{\partial t} + \nabla \cdot (\phi_s \mathbf{v}_s) = 0, \tag{A.22}$$

$$\nabla \cdot (\phi_s \mathbf{v}_s + \phi_f \mathbf{v}_f) = 0, \tag{A.23}$$

$$\nabla \cdot (\phi_f \boldsymbol{\sigma}_f) - \phi_f \nabla p + \xi C a \phi_f \phi_s (\mathbf{v}_s - \mathbf{v}_f) = 0, \tag{A.24}$$

$$\nabla \cdot (\phi_s \sigma_s) - \phi_s \nabla p + \xi Ca \phi_f \phi_s (\mathbf{v}_f - \mathbf{v}_s) = 0, \tag{A.25}$$

$$\frac{d\mathbf{u}_s}{dt} - \mathbf{v}_s = 0,\tag{A.26}$$

$$\nabla \cdot \mathbf{V} = 0, \tag{A.27}$$

$$\nabla \cdot \mathbf{\Sigma} - \nabla P = 0, \tag{A.28}$$

$$\Sigma = Ca(\nabla \mathbf{V} + \nabla \mathbf{V}^T),\tag{A.29}$$

$$\nabla \cdot \boldsymbol{\sigma}_c = 0, \tag{A.30}$$

$$\boldsymbol{\sigma}_f = Ca(\nabla \mathbf{v}_f + \nabla \mathbf{v}_f^T),\tag{A.31}$$

$$\sigma_s = J^{-1}(\mathbf{F} \cdot \mathbf{F}^T - \mathbf{I}) + \lambda_s(J - 1)\mathbf{I}.$$
 (A.32)

The dimensionless boundary conditions appear the same as the dimensional ones given in Section A.2, except for the following corresponding to Eqs. (A.15–A.17) on the gel-fluid interface:

$$Ca(\mathbf{V} - \mathbf{v}_f) \cdot \mathbf{n} = \eta \, \mathbf{n} \cdot [(\mathbf{\Sigma} - P\mathbf{I}) - (\boldsymbol{\sigma}_s - p\mathbf{I})] \cdot \mathbf{n}.$$
 (A.33)

$$Ca(\mathbf{V} - \mathbf{v}_f) \cdot \mathbf{t} = \beta(\mathbf{\Sigma} \cdot \mathbf{n}) \cdot \mathbf{t},$$
 (A.34)

$$Ca \phi_s(\mathbf{v}_s - \mathbf{v}_f) \cdot \mathbf{t} = -\beta (\boldsymbol{\sigma}_s \cdot \mathbf{n}) \cdot \mathbf{t}. \tag{A.35}$$

# Appendix B Parameter estimation

Most of the model parameters can be estimated from typical material properties and experimental devices. In presenting results in the main text, we have omitted the overbar for dimensionless groups since the discussion does not concern dimensional parameters. In this appendix, however, both types are present as we will first estimate the dimensional parameters before evaluating the dimensionless groups. Thus, we revert temporarily to using an overbar to distinguish dimensionless parameters from dimensional ones.

Initial solid fraction: Many hydrogels have high porosity, with a swelling ratio reaching 40 or higher (corresponding to solid fraction of 2.5% or lower) [38]. We have taken the initial solid fraction  $\phi_{s0} = 0.01$  for an initial 99% porosity [39].

Elastic moduli: Hydrogels can have a wide range of stiffness, with Young's modulus E ranging from hundreds of pascals to tens of kPa [6]. The Poisson ratio  $\nu$  has been reported to be about 0.2 [40] or 0.33 [41]. For simplicity, we choose  $\nu=0.25$  such that the two Lamé constants are equal (see Eq. A.7). However, the experiments measured the response of the entire hydrogel, including both the solid and the liquid. In the notation of our BC (Eq. A.14), they measured  $P-p=\phi_s\sigma_s$ . Thus, a measured  $E_m=10^3$  Pa translates to  $E=E_m/\phi_s=10^5$  Pa in our constitutive equation (Eqs. A.6, A.7). This further translates to  $\lambda_s=\mu_s=4\times10^4$  Pa.

Biological cells also exhibit a wide range of stiffness, with a Young's modulus ranging from 100 Pa up to tens of kPa [42,43]. These values are largely comparable to those of hydrogels. In all the simulations presented, we have matched the cell moduli with those of the surrounding gel at solid fraction  $\phi_s = 0.01$ :  $\mu_c = \lambda_c = 0.01 \mu_s = 0.01 \lambda_s$ . Thus, we have the following baseline values for the dimensionless groups:  $\bar{\lambda}_s = 1$ ,  $\bar{\lambda}_c = \bar{\mu}_c = 0.01$ , and a Poisson ratio for the cell  $\nu_c = 0.25$ .

Darcy drag coefficient:  $\xi$  appears in the momentum equation, which, if written in the traditional Darcy's law or Brinkman's form, involves the bulk permeability k. Comparing these two forms establishes the following connection:

$$\xi = \frac{\mu}{k} \frac{\phi_f}{\phi_s},\tag{B.1}$$

so that  $\xi$  can be evaluated from the more familiar parameter k. In particular, we adopt the Darcy permeability formula suitable for high porosity media [44,45]:

$$k = \frac{2r^2}{9} \frac{\phi_f}{\phi_s},\tag{B.2}$$

where r is a characteristic pore radius, which falls in the wide range of 0.1–100  $\mu m$  for hydrogels [11–13]. Thus,  $\xi = 4.5 \mu/r^2$ . Taking  $\mu = 10^{-3}$  Pa·s for water, and r = 2.5  $\mu m$  as a typical pore size, we get  $\xi = 7.2 \times 10^8$  kg/(m³·s). The dimensionless group  $\bar{\xi} = \xi L_0^2/\mu = 4.5(L_0/r)^2$  is directly related to the pore-to-sample size ratio. The macroscopic size of the devices ranges from hundreds of microns to millimeters [14,15]. Taking r = 2.5  $\mu m$  and  $L_0 = 250$   $\mu m$ , we get  $\bar{\xi} = 4.5 \times 10^4$ .

Interfacial permeability and slip coefficients: The boundary condition BC2 introduces the permeability  $\eta$  via Eq. (A.15), which can be rewritten as

$$\mu \frac{(\mathbf{V} - \mathbf{v}_f) \cdot \mathbf{n}}{\mu \eta} = \mathbf{n} \cdot [(\mathbf{\Sigma} - P\mathbf{I}) - (\boldsymbol{\sigma}_s - p\mathbf{I})] \cdot \mathbf{n}, \tag{B.3}$$

Dimensionless groups	Baseline values
e	1.2
$\phi_{s_0}$	0.01
$\lambda_s$	1
$\lambda_c$	0.01
$\mu_c$	0.01
ξ	$4.5 \times 10^{4}$
β	0.02
$\eta$	0.02
Ca	$3 \times 10^{-11}$

Table 1: Baseline values for the dimensionless parameters used in the shear-flow and normal-flow simulations.

which gives the quantity  $\mu\eta$  the meaning of a "penetration length", i.e., the depth into the gel over which the fluid's normal velocity changes from  $\mathbf{V}$  to  $\mathbf{v}_f$ . This idea has been explored in a pore-scale model, which shows that for hydrogels, this penetration length ranges from r to 4r [21]. Taking an intermediate value of 2r, we get the dimensionless  $\bar{\eta} = \mu\eta/L_0 = 2r/L_0 = 0.02$  for  $r = 2.5 \ \mu\text{m}$ ,  $L_0 = 250 \ \mu\text{m}$ .

Similarly, the dimensionless slip coefficient  $\bar{\beta} = \mu \beta/L_0$  can be seen as the slip length divided by the macroscopic length scale. Prior calculations showed that shear flow past the surface of a porous medium entrains the interstitial fluid down to a depth on the order of 2r [46]. This yields  $\bar{\beta} = 0.02$ .

Capillary number: In their experimental device, Polacheck *et al.* [14] tested interstitial velocities  $v_f = 0.3 \ \mu\text{m/s}$  and  $3 \ \mu\text{m/s}$ . Because of the high porosity of typical hydrogels (0.9 or higher), the free-stream velocity  $V_0$  should be only slightly smaller than  $v_f$ . Thus, we adopt  $V_0 = 0.3 \ \mu\text{m/s}$  as a representative velocity. With the length  $L_0 = 0.25 \ \text{mm}$  typical of microfluidic devices,  $\mu = 10^{-3} \ \text{Pa·s}$ , and  $\mu_s = 4 \times 10^4 \ \text{Pa}$ , we obtain  $Ca = \mu V_0/(\mu_s L_0) = 3 \times 10^{-11}$  for our normal-flow geometry.

Based on the above, we have chosen the baseline dimensionless parameters in Table 1, which are used in all the results reported in the main text. The different simulations correspond to different configurations of the cell array and different values of the cell-cell separation h.

# References

- [1] M. W. Tibbitt, K. S. Anseth, Hydrogels as extracellular matrix mimics for 3D cell culture, Biotechnol. Bioeng. 103 (4) (2009) 655–663.
- [2] V. van Duinen, S. J. Trietsch, J. Joore, P. Vulto, T. Hankemeier, Microfluidic 3D cell culture: from tools to tissue models, Curr. Opin. Biotechnol. 35 (2015) 118–126.
- [3] H. Liu, Y. Wang, K. Cui, Y. Guo, X. Zhang, J. Qin, Advances in hydrogels in organoids and organs-on-a-chip, Adv. Mater. 31 (50) (2019) 1902042.
- [4] L. A. Low, C. Mummery, B. R. Berridge, C. P. Austin, D. A. Tagle, Organs-on-chips: into the next decade, Nat. Rev. Drug Discov. 20 (2021) 345–361.
- [5] A. Löwa, J. J. Feng, S. Hedtrich, Human disease models in drug development, Nat. Rev. Bioeng. 1 (2023) 545–559.
- [6] D. Lee, H. Zhang, S. Ryu, Elastic modulus measurement of hydrogels, in: M. I. H. Mondal (Ed.), Cellulose-Based Superabsorbent Hydrogels, Springer International Publishing, Cham, 2018, pp. 1–21.
- [7] J. Y. Park, J. B. White, N. Walker, C.-H. Kuo, W. Cha, M. E. Meyerhoff, S. Takayama, Responses of endothelial cells to extremely slow flows, Biomicrofluidics 5 (2) (2011) 022211.
- [8] X. Zhang, S. Zhang, T. Wang, How the mechanical microenvironment of stem cell growth affects their differentiation: a review, Stem Cell Res. Ther. 13 (2022) 415.
- [9] Y. Du, N. Li, H. Yang, C. Luo, Y. Gong, C. Tong, Y. Gao, S. Lü, M. Long, Mimicking liver sinusoidal structures and functions using a 3d-configured microfluidic chip, Lab Chip 17 (2017) 782–794.
- [10] W. Li, Y. Wu, W. Hu, J. Zhou, X. Shu, X. Zhang, Z. Zhang, H. Wu, Y. Du, D. Lü, S. Lü, N. Li, M. Long, Direct mechanical exposure initiates hepatocyte proliferation, JHEP Rep. 5 (2023) 100905.
- [11] Y.-C. Chiu, M.-H. Cheng, H. Engel, S.-W. Kao, J. C. Larson, S. Gupta, E. M. Brey, The role of pore size on vascularization and tissue remodeling in PEG hydrogels, Biomaterials 32 (26) (2011) 6045–6051.

- [12] A. Salerno, R. Borzacchiello, P. A. Netti, Pore structure and swelling behavior of porous hydrogels prepared via a thermal reverse-casting technique, J. Appl. Polym. Sci. 122 (2011) 3651–3660.
- [13] S. Sornkamnerd, M. K. Okajima, T. Kaneko, Tough and porous hydrogels prepared by simple lyophilization of LC gels, ACS Omega 2 (8) (2017) 5304–5314.
- [14] W. J. Polacheck, J. L. Charest, R. D. Kamm, Interstitial flow influences direction of tumor cell migration through competing mechanisms, Proc. Natl. Acad. Sci. U. S. A 108 (27) (2011) 11115–11120.
- [15] B. Bachmann, S. Spitz, M. Rothbauer, C. Jordan, M. Purtscher, H. Zirath, P. Schuller, C. Eilenberger, S. F. Ali, S. Mühleder, E. Priglinger, M. Harasek, H. Redl, W. Holnthoner, P. Ertl, Engineering of three-dimensional pre-vascular networks within fibrin hydrogel constructs by microfluidic control over reciprocal cell signaling, Biomicrofluidics 12 (4) (2018) 042216.
- [16] C. M. Novak, E. N. Horst, C. C. Taylor, C. Z. Liu, G. Mehta, Fluid shear stress stimulates breast cancer cells to display invasive and chemoresistant phenotypes while upregulating PLAU in a 3D bioreactor, Biotechnol. Bioeng. 116 (11) (2019) 3084–3097.
- [17] L. Li, J. Zhang, Z. Xu, Y.-N. Young, J. J. Feng, P. Yue, An arbitrary Lagrangian-Eulerian method for simulating interfacial dynamics between a hydrogel and a fluid, J. Comput. Phys. 451 (2022) 110851.
- [18] L. Li, J. Zhang, P. Yue, J. J. Feng, Mechanical interaction between a hydrogel and an embedded cell in biomicrofluidic applications, Biomicrofluidics 19 (2025) 024104.
- [19] J. J. Feng, Y.-N. Young, Boundary conditions at a gel-fluid interface, Phys. Rev. Fluids 5 (12) (2020) 124304.
- [20] Z. Xu, J. Zhang, Y.-N. Young, P. Yue, J. J. Feng, A comparison of four boundary conditions for the fluid-hydrogel interface, Phys. Rev. Fluids 7 (2022) 093301.
- [21] Z. Xu, P. Yue, J. J. Feng, Estimating the interfacial permeability for flow into a poroelastic medium, Soft Matter 20 (2024) 7357–7361.

- [22] D. Arndt, W. Bangerth, M. Bergbauer, M. Feder, M. Fehling, J. Heinz, T. Heister, L. Heltai, M. Kronbichler, M. Maier, et al., The deal.II library, version 9.5, J. Num. Math. 31 (3) (2023) 231–246.
- [23] T. Miyazaki, H. Hasimoto, Separation of creeping flow past two circular cylinders, J. Phys. Soc. Jpn. 49 (1980) 1611–1618.
- [24] H. Hasimoto, O. Sano, Stokeslets and eddies in creeping flow, Ann. Rev. Fluid Mech. 12 (1980) 335–363.
- [25] Y. Shou, X. Y. Teo, K. Z. Wu, B. Bai, A. R. K. Kumar, J. Low, Z. Le, A. Tay, Dynamic stimulations with bioengineered extracellular matrixmimicking hydrogels for mechano cell reprogramming and therapy, Adv. Sci. 10 (21) (2023) 2300670.
- [26] D. Brindley, K. Moorthy, J. H. Lee, C. Mason, H. W. Kim, I. Wall, Bioprocess forces and their impact on cell behavior: implications for bone regeneration therapy, J. Tissue Eng. 2011 (2011) 620247.
- [27] F. Friedland, S. Babu, R. Springer, J. Konrad, Y. Herfs, S. Gerlach, J. Gehlen, H.-J. Krause, L. De Laporte, R. Merkel, E. Noetzel, ECMtransmitted shear stress induces apoptotic cell extrusion in early breast gland development, Front. Cell Dev. Biol. 10 (2022) 947430.
- [28] K. Duval, H. Grover, L.-H. Han, Y. Mou, A. F. Pegoraro, J. Fredberg, Z. Chen, Modeling physiological events in 2D vs. 3D cell culture, Physiology 32 (4) (2017) 266–277.
- [29] L. Figueiredo, R. Pace, C. D'Arros, G. Réthoré, J. Guicheux, C. Le Visage, P. Weiss, Assessing glucose and oxygen diffusion in hydrogels for the rational design of 3D stem cell scaffolds in regenerative medicine, J. Tissue Eng. Regen. Med. 12 (5) (2018) 1238–1246.
- [30] M. E. Dolega, S. Monnier, B. Brunel, J.-F. Joanny, P. Recho, G. Cappello, Extracellular matrix in multicellular aggregates acts as a pressure sensor controlling cell proliferation and motility, eLife 10 (2021) e63258.
- [31] A. Liu, M. Islam, N. Stone, V. Varadarajan, J. Jeong, S. Bowie, P. Qiu, E. K. Waller, A. Alexeev, T. Sulchek, Microfluidic generation of transient cell volume exchange for convectively driven intracellular delivery of large macromolecules, Mater. Today 21 (7) (2018) 703-712.

- [32] A. Liu, T. Yu, K. Young, N. Stone, S. Hanasoge, T. J. Kirby, V. Varadarajan, N. Colonna, J. Liu, A. Raj, J. Lammerding, A. Alexeev, T. Sulchek, Cell mechanical and physiological behavior in the regime of rapid mechanical compressions that lead to cell volume change, Small 16 (2) (2020) 1903857.
- [33] L. R. Smith, S. Cho, D. E. Discher, Stem cell differentiation is regulated by extracellular matrix mechanics, Physiology 33 (1) (2018) 16–25.
- [34] H. Lv, L. Li, S. M., Y. Zhang, L. Chen, Y. Rong, Y. Li, Mechanism of regulation of stem cell differentiation by matrix stiffness, Stem Cell Res. Ther. 6 (1) (2015) 103.
- [35] P. Lu, K. Takai, V. M. Weaver, Z. Werb, Extracellular matrix degradation and remodeling in development and disease, Cold Spring Harb. Perspect. Biol. 3 (12) (2011) a005058.
- [36] R. Fickentscher, P. Struntz, M. Weiss, Mechanical cues in the early embryogenesis of *Caenorhabditis elegans*, Biophys. J. 105 (8) (2013) 1805–1811.
- [37] D. N. Alasaadi, R. Mayor, Mechanically guided cell fate determination in early development, Cell. Mol. Life Sci. 81 (2024) 242.
- [38] N. Annabi, J. W. Nichol, X. Zhong, C. Ji, S. Koshy, A. Khademhosseini, F. Dehghani, Controlling the porosity and microarchitecture of hydrogels for tissue engineering, Tissue Eng. Part B 16 (4) (2010) 371–383.
- [39] N. L. Cuccia, S. Pothineni, B. Wu, J. Méndez Harper, J. C. Burton, Pore-size dependence and slow relaxation of hydrogel friction on smooth surfaces, Proc. Natl. Acad. Sci. U. S. A 117 (21) (2020) 11247–11256.
- [40] Y.-N. Young, Y. Mori, M. J. Miksis, Slightly deformable Darcy drop in linear flows, Phys. Rev. Fluids 4 (2019) 063601.
- [41] J. Yoon, S. Cai, Z. Suo, R. C. Hayward, Poroelastic swelling kinetics of thin hydrogel layers: comparison of theory and experiment, Soft Matter 6 (23) (2010) 6004.
- [42] M. J. Jembrek, G. Šimić, P. R. Hof, S. Šegota, Atomic force microscopy as an advanced tool in neuroscience, Transl. Neurosci. 6 (1) (2015) 117–130.

- [43] Q. Luo, D. Kuang, B. Zhang, G. Song, Cell stiffness determined by atomic force microscopy and its correlation with cell motility, Biochim. Biophys. Acta, Gen. Subj. 1860 (9) (2016) 1953–1960.
- [44] Z. Xu, P. Yue, J. J. Feng, Hystereses in flow-induced compression of a poroelastic hydrogel, Soft Matter 20 (2024) 6940–6951.
- [45] Z. Xu, P. Yue, J. J. Feng, A theory of hydrogel mechanics that couples swelling and external flow, Soft Matter 20 (2024) 5389–5406.
- [46] D. F. James, A. M. Davis, Flow at the interface of a model fibrous porous medium, J. Fluid Mech. 426 (2001) 47–72.